



All Theses and Dissertations

2012-02-17

Measurement of Plasma Density in a Gas-Filled Ionizing Laser Focus

Nathan Edward Heilmann
Brigham Young University - Provo

Follow this and additional works at: <https://scholarsarchive.byu.edu/etd>

 Part of the [Astrophysics and Astronomy Commons](#), and the [Physics Commons](#)

BYU ScholarsArchive Citation

Heilmann, Nathan Edward, "Measurement of Plasma Density in a Gas-Filled Ionizing Laser Focus" (2012). *All Theses and Dissertations*. 2947.

<https://scholarsarchive.byu.edu/etd/2947>

This Thesis is brought to you for free and open access by BYU ScholarsArchive. It has been accepted for inclusion in All Theses and Dissertations by an authorized administrator of BYU ScholarsArchive. For more information, please contact scholarsarchive@byu.edu, ellen_amatangelo@byu.edu.

Measurement of Plasma Density in a Gas-Filled Ionizing Laser Focus

Nathan Heilmann

A thesis submitted to the faculty of
Brigham Young University
in partial fulfillment of the requirements for the degree of
Master of Science

Scott Bergeson, Chair
Justin Peatross
Michael Ware

Department of Physics and Astronomy

Brigham Young University

April 2012

Copyright © 2012 Nathan Heilmann

All Rights Reserved

ABSTRACT

Measurement of Plasma Density in a Gas-Filled Ionizing Laser Focus

Nathan Heilmann
Department of Physics and Astronomy
Master of Science

We use an interferometric method for measuring the plasma density in a laser-induced plasma as a function of time. Any changes in the density within 5 ns of generation is due plasma expansion and not recombination. The analytic solution for plasma expansion derived for ultracold Neutral Plasmas describes the expansion of our laser produced Neon plasma of densities up to approximately 40 Torr. A model for the ultracold neutral plasmas, in comparison with measurements of our plasmas, can be used to extract an electron temperature. Currently our plasmas have shown to have an electron temperature of approximately 44 eV.

Keywords: Laser-produced plasmas, atomic physics, ultracold neutral plasmas, interferometry

ACKNOWLEDGMENTS

I would like to acknowledge Justin Peatross and Scott Bergeson for all of their support and assistance. Also, thank you to all of the students from the high harmonics research group at BYU for their contribution to past research and contribution for this research. I would also like to thank the National Science Foundation for supporting this research (Grant Numbers PHY-0969856 and PHY-0457316).

Contents

Table of Contents	iv
List of Figures	v
1 Introduction	1
1.1 Laser-Produced Plasma	1
1.2 Electron Temperature Measurements	3
1.3 Overview of Thesis	4
2 Theory of EM-Wave Propagation in a Plasma	7
2.1 Free Electron Index of Refraction	7
2.2 Two-slit Interferometry	8
3 Experimental Setup	11
3.1 The Femtosecond Laser System	11
3.2 Vacuum System and Gas Jet	15
3.3 System Electronics	17
3.4 A Gas Cell for Calibration Purposes	19
3.5 Data Acquisition	21
4 Data Analysis and Discussion	23
4.1 The Analysis Matlab Program	23
4.2 Results	25
4.3 Conclusion	29
Bibliography	31
Index	32
A Matlab - Data Analysis	32

List of Figures

1.1	The Coulomb Potential Well Distorted by the Strong-Laser Field	2
1.2	Comparison of Kanter with UNP model	5
2.1	Michelson Interferometer	9
3.1	Optical Setup	12
3.2	The foci as seen by the diagnostic CCD	13
3.3	The foci positions relative to each other and the Gas Jet	14
3.4	Vacuum Chamber	16
3.5	Schematic of the Vacuum Chamber	16
3.6	Gas Jet Modification	17
3.7	Gas Jet in Chamber	18
3.8	Gas Cell Setup	19
3.9	Gas Cell	20
3.10	Ionized VS. Non-Ionized Interference Fringes	21
4.1	Plots of the Compared Data and Fringe Position	24
4.2	Plots of the Fringe/Phase Change Over Time	26
4.3	Comparison of Data with UNP model	28

Chapter 1

Introduction

1.1 Laser-Produced Plasma

Laser-produced plasmas (LPPs) span a wide range of temperatures and densities [1]. Many of the early LPP experiments were designed to generate fusion conditions with densities near $n = 10^{29} \text{ m}^{-3}$. The highest intensity LPP experiments now generate electrons with temperatures up to $T_e = 400 \text{ MeV}$ using relativistic wakefield acceleration [2]. In contrast, the temperature and density in more recent ultracold plasma experiments are in the range of $T_e = 1 \text{ K}$ and $n = 10^{16} \text{ m}^{-3}$ [3].

In the strong-field regime, atoms undergo ionization when the laser field is stronger than the Coulomb attraction from the nucleus. In this regime, one can estimate the intensity necessary for ionization using a one dimensional coulomb potential. The strong laser field adds the term exE where E is the electric field from the laser. The total potential is then

$$U = \frac{-e^2}{4\pi\epsilon_0 x} - exE \quad (1.1)$$

which describes a distorted Coulomb potential well that binds the electron. The shape of the potential at a moment when the laser field is strong is shown in Fig. 1.1. If the barrier is sufficiently suppressed, the electron can escape from the Coulomb well. To find a peak of the barrier, or zero

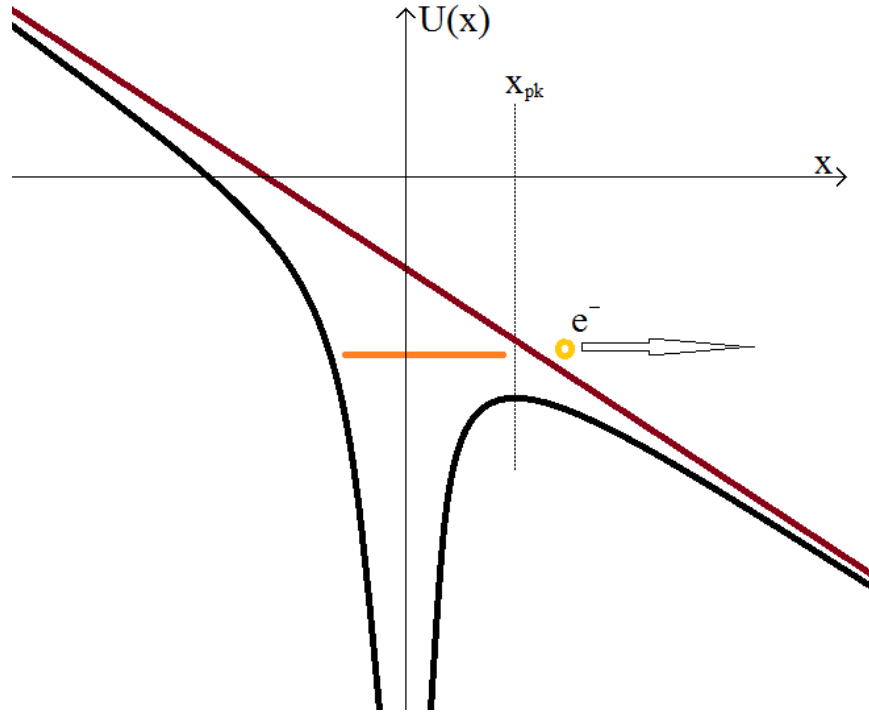


Figure 1.1 The laser distorted Coulomb potential well for a bound electron.

slope location, a derivative is set to zero:

$$-\frac{dU}{dx} = \frac{e^2}{4\pi\epsilon_0 x^2} - eE = 0 \quad \Longrightarrow \quad x_{pk} = \sqrt{\frac{e}{4\pi\epsilon_0 E}} \quad (1.2)$$

We find the height of the barrier by plugging this value for x back into Eq. (1.1) to find

$$U_{pk} = \frac{-2e^{3/2}\sqrt{E}}{\sqrt{4\pi\epsilon_0}} \quad (1.3)$$

If the energy of the bound electron is greater than this peak potential, then the electron is able to escape the atom under the influence of the laser field.

We can find the field strength (or laser intensity) necessary for ionization by requiring the peak barrier height to equal the binding energy: $\Phi = U_{pk}$. We substitute the formula $I = \frac{\epsilon_0 c}{2} E^2$ into Eq. (1.3) to get an equation relating the binding energy directly to the laser intensity:

$$\Phi = \frac{-2e^{3/2}\left(\frac{2I}{\epsilon_0 c}\right)^{1/4}}{\sqrt{4\pi\epsilon_0}}. \quad (1.4)$$

Solving this equation for intensity instead of potential, we can determine at which intensity the laser will ionize the atom,

$$I \geq \frac{c\pi^2\epsilon_0^3}{2e^6}\Phi^4 = 4.0 \times 10^9 \frac{\text{W}}{\text{cm}^2\text{eV}^4} \frac{\Phi^4}{Z^2}, \quad (1.5)$$

where Φ is the binding energy, and Z is the ionization state. To ionize neon, which has a binding energy of 21.564eV, a laser intensity greater than 8.7×10^{14} W/cm² is required.

1.2 Electron Temperature Measurements

One of the interesting and difficult-to-determine characteristics of LPPs produced in the strong-field limit is the electron temperature [4]. In directly photo-ionized plasmas, the electron energy is given by the photoelectric equation

$$E_e = h\nu - \Phi. \quad (1.6)$$

However, in strong-field ionization, the electron temperature (1 eV of electron energy corresponds to 11600 K) is more complicated and is usually calculated using the Vlasov equations [5]. An initial electron distribution function is assumed, the plasma evolution is simulated, measurable quantities are extracted from the simulation, and these quantities are compared with experimental measurements [6]. The process is repeated with different assumed distributions until a reasonable agreement between the simulation and experiment is reached.

In an LPP, the initial free electron spatial distribution is highly localized and confined by the space-charge of the ions. The electrons have excess kinetic energy and oscillate in the electrostatic potential resulting from the ion space-charge. As the electrons try to escape, they hit the wall of this trap and are ‘pulled’ back. The force exerted by the electrons on the ions results in a pressure that causes the plasma to expand. The Coulomb repulsion between ions is negligible due to the low density of the gas jet, where the spacing between the ions is great enough that the effects from the electrons are overpowering.

A recent publication by Kanter [6] shows how numerical simulations can be used to find the electron temperature. Using resonant x-ray absorption measurements, they determine the density of their LPP as a function of time. Using the Vlasov equations [5] they simulate the plasma expansion for different initial electron temperatures. They compare the simulations of ion spatial distributions against their measured densities to determine the initial temperature in their plasma.

The Kanter data can also be analyzed by using a model initially developed for ultracold neutral plasmas (UNPs). In contrast to LPPs, the Vlasov equations for UNPs have analytic solutions because the spacial density distribution is Gaussian and expands in a self-similar manner. The Vlasov equations are valid in the limit that the number of particles per Debye sphere satisfies $N\lambda_D^3 \gg 1$, where $\lambda_D = \sqrt{k_B T_e \epsilon_0 / Ne^2}$. For a typical LPP, such as Kanter's [6], with $N = 10^{20} \text{ m}^{-3}$ and $T_e = 5 \text{ eV}$, we have $N\lambda_D^3 = 500 \gg 1$. We might therefore expect the UNP solution to be valid for the LPP.

In Fig. 1.2 we compare the data from Kanter [6] with the UNP solution. Note that the UNP solution is close to Kanter's numerical simulation. It appears to be a good fit to the experimental data, suggesting that if the plasma density is known that the UNP model could provide a simple method to determine the electron temperature. To our knowledge, this direct comparison has not been previously made. The details of the UNP model will be discussed later in this thesis.

1.3 Overview of Thesis

In this thesis we demonstrate a new interferometric method for measuring plasma density in a gas-filled laser focus as a function of time after interaction with the ultrashort pulse. We use this method to measure the density in an LPP for a range of initial densities and over a time range of about 5 ns. We show that the plasma density is well-modeled using the UNP analytic solutions and suggest ways this could be used to explore the dependence of the electron temperature on the

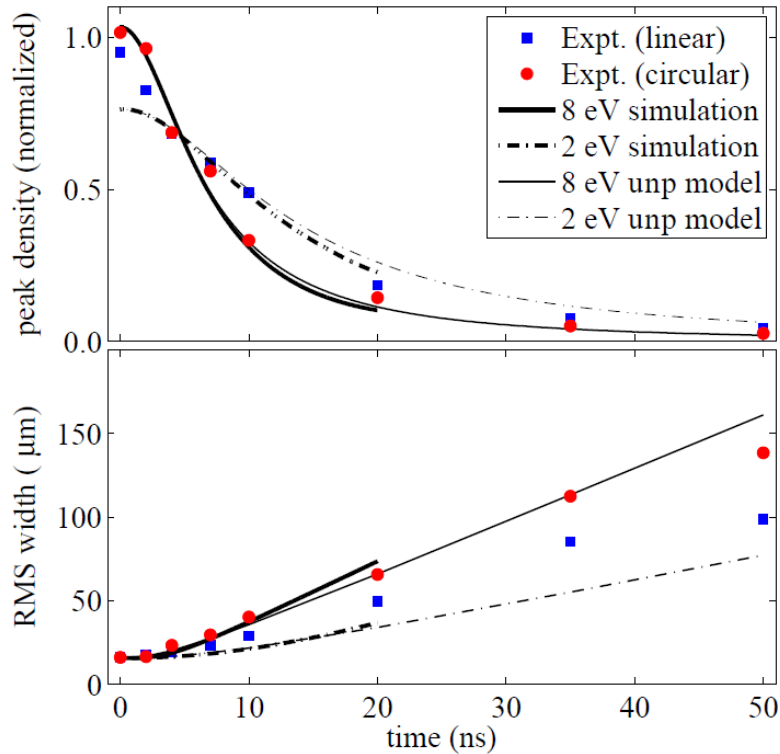


Figure 1.2 A comparison of the data and models of Kanter [6] with the ultracold plasma expansion model. The blue squares are measured data when the fs laser is linearly polarized. The red circles are measured when the fs laser is circularly polarized. The dark lines running from 1 to 20 ns are the simulation from Ref. [6]. The thin lines running from 1 to 50 ns are the UNP model predictions. Top Panel: LPP peak density as a function of time for two different laser polarizations. At times before 4 ns, the blue squares are much higher than the model because of an alignment effect. Bottom Panel: LPP rms width. The UNP model closely follows the simulation and provides a simple formula that can be used to extract the electron temperature.

laser parameters.

The interferometer uses an 800 nm, 35 fs, pulsed laser beam divided into three separate and temporally coherent laser beams. The strongest of the laser beams is used to generate plasma. The two weaker beams are used to measure the plasma density. A variable optical delay line is used to temporally delay these two weaker beams. One of the weaker beams, the ‘probe’ beam, passes through the plasma. The other, the ‘reference’ beam, passes next to the plasma. The probe beam experiences a phase delay due to the plasma’s index of refraction. By measuring the relative phase of these two beams, we can calculate the index of refraction and therefore the plasma density as a function of time. Then using the UNP model we can extract the electron temperature.

Chapter 2

Theory of EM-Wave Propagation in a Plasma

2.1 Free Electron Index of Refraction

We measure the plasma density by calculating its index of refraction, based on the Lorentz Model. This model treats each electron as a classical particle obeying Newton's second law. We assume that only the free electrons contribute to the index of refraction. When ionized, we treat the electrons as having no interactions with neighboring ions or other electrons (i.e. no restoring forces or collisions). The model assumes that the electrons are uniformly distributed throughout space. This model is used to determine the susceptibility of the plasma $\chi(\omega)$, which in turn can be used to calculate the index via

$$(n + i\kappa)^2 = 1 + \chi(\omega) \quad (2.1)$$

Following Newton's second law, the forces acting on the atoms matches the electron mass times its acceleration:

$$m_e \ddot{x}_e = q_e E \quad (2.2)$$

where $q_e E$ is the force from an external electric field and m_e is the mass and \ddot{r}_e is the acceleration. Assuming a simple sinusoidal force $E e^{i(k \cdot r - \omega t)}$, the resulting solution to Eq. (2.2) is:

$$r_e = \frac{q_e E_0 e^{i(k \cdot r - \omega t)}}{m_e (-\omega^2)} \quad (2.3)$$

We can now use Eq. (2.3) to write out the polarization in terms of the electric field. By comparing two well-known forms of the polarization equation, $P_0(\omega) = \epsilon_0 \chi(\omega) E_0(\omega)$ and $P = N q_e r_{micro}$, we can find the susceptibility in terms of the plasma density. At position zero we get:

$$\epsilon_0 \left(\frac{\omega_p^2}{-\omega^2} \right) E_0 = \epsilon_0 \chi(\omega) E_0(\omega) \quad (2.4)$$

where $\omega_p = \sqrt{\frac{N q_e^2}{\epsilon_0 m_e}}$ is the plasma frequency. The susceptibility of a plasma can be written as

$$\chi(\omega) = \frac{\omega_p^2}{-\omega^2} \quad (2.5)$$

We are then left with the completely real index for an electron cloud.

$$n = \sqrt{1 - \frac{\omega_p^2}{\omega^2}} \quad (2.6)$$

With $\omega = \frac{2\pi c}{\lambda}$ and the plasma frequency described previously, we get the equation:

$$n = \sqrt{1 - \frac{N e^2 \lambda^2}{4\pi^2 \epsilon_0 m c^2}} \simeq 1 - \frac{1}{2} \frac{N e^2 \lambda^2}{4\pi^2 \epsilon_0 m c^2} \dots \quad (2.7)$$

2.2 Two-slit Interferometry

Our interferometric method measures the relative phase of two low-intensity laser beams. We use a Michelson interferometer to generate these two beams. The interferometer is used in its standard configuration with one change. One of the interferometer mirrors is tilted by a small angle θ .

Because of this, the two beams emerge on slightly different paths instead of both beams traveling the same path after the beamsplitter. Because of the law of reflection their angular separation

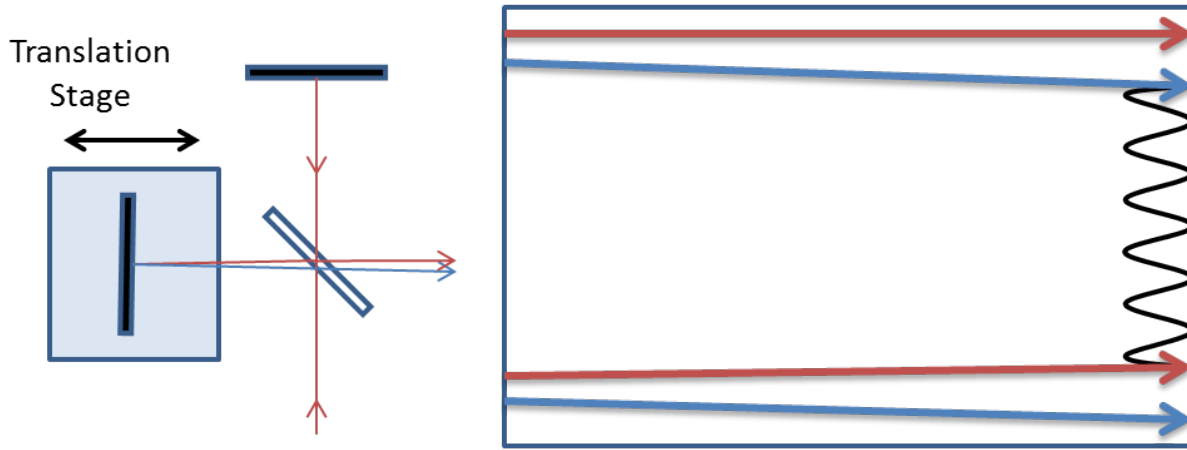


Figure 2.1 Diagram of a basic Michelson Interferometer which has been misaligned on one mirror by a small angle so the resulting beams diverge slightly (divergence has been exaggerated in the diagram to allow representation). The part on the right depicts how the interference fringes show only where the two beams overlap.

is twice the misalignment angle of the interferometer mirror. Although the beams exit the interferometer traveling on two slightly different paths, they overlap spatially. The laser beam diameter is approximately 1 cm and the angular deviation of the two beams in our setup is 3 mRad.

As discussed later in this thesis, these two beams are focused into the vacuum chamber. At the focus of the lens, these two laser beams form well-separated focal spots. However as the laser beams propagate after the focus, they diverge so that in the far field the two laser beams overlap again. They form interference fringes similar to those of Young's two-slit pattern. The intensity pattern of these these fringes can be written as

$$I_{tot} = 2I_0\{1 + \cos[kx \sin(2\theta) + \phi]\} \quad (2.8)$$

In this equation ϕ is a relative phase difference between the two beams, and for our purposes we are most interested in the this value and the way it changes.

The misalignment of the two beams needs to be sufficiently large to produce easily observable fringes, but still small enough so the two beams overlap. Then fringes are formed from the interference of the two beams as they propagate. The fringe position in x depends on the relative phase

between the two beams.

The relative phase between the two beams arises when the probe beam passes through the plasma while the reference propagates in vacuum. As the index changes in time, the fringes in the interference pattern shift as a function of pulse delay. The fringe shift is a measure of the relative phase delay in the two weak laser beams. The change in the phase delay from Eq. (2.8) becomes

$$\Delta\phi = 2\pi\frac{L}{\lambda}(1-n) \approx \frac{LN e^2 \lambda^2}{4\pi\epsilon_0 m c^2} \quad (2.9)$$

This shift is entirely dependent on the plasma index and also the path length L through the plasma. When the path length is known, the index can be calculated from the fringe shifts.

The index of refraction for the plasma changes as the plasma density changes. We can change the density by selecting the backing pressure of the gas jet. But the density also changes as the plasma expands in time, which can be observed by delaying the probe and reference beams together relative to the ionizing laser beam and observing the change in the fringe shift.

Chapter 3

Experimental Setup

3.1 The Femtosecond Laser System

Pulses in our laser system originate in a self-modelocking oscillator (KM labs) pumped by a 5 W continuous laser at 532 nm (Coherent 5 W Verdi). Pulses emerge from the oscillator every 11 ns with about 1 nJ energy. These are stretched to 100 ps in a grating setup, after which a Pockels cell selects a single pulse for amplification each 0.1 s. The selected pulses enter a sequence of Ti:sapphire multipass-amplifiers pumped by 600 mJ of pulsed 532 nm light at 10 Hz (QuantaRay 230 Pro). The pulses reach an energy of 50 mJ before being re-compressed to about 35 fs.

Our experimental setup allows us to vary the time delay between the strong laser beam, which generates the plasma, and the two weak laser beams, which are used to measure the plasma density. Using the high-power 800 nm laser system, a pulse of the laser is split by a 95:5 beam splitter (beamsplitter1 in Fig. 3.1). The stronger beam, referred to as the ‘ionizing beam’, travels directly to the experiment with an appropriate delay path. It encounters a 50:50 beam splitter before entering the vacuum chamber through a 50 cm lens. A 1/2 inch diameter iris is used to make the beam width of the ionizing beam smaller than the weaker beam so its focal spot is larger. This is

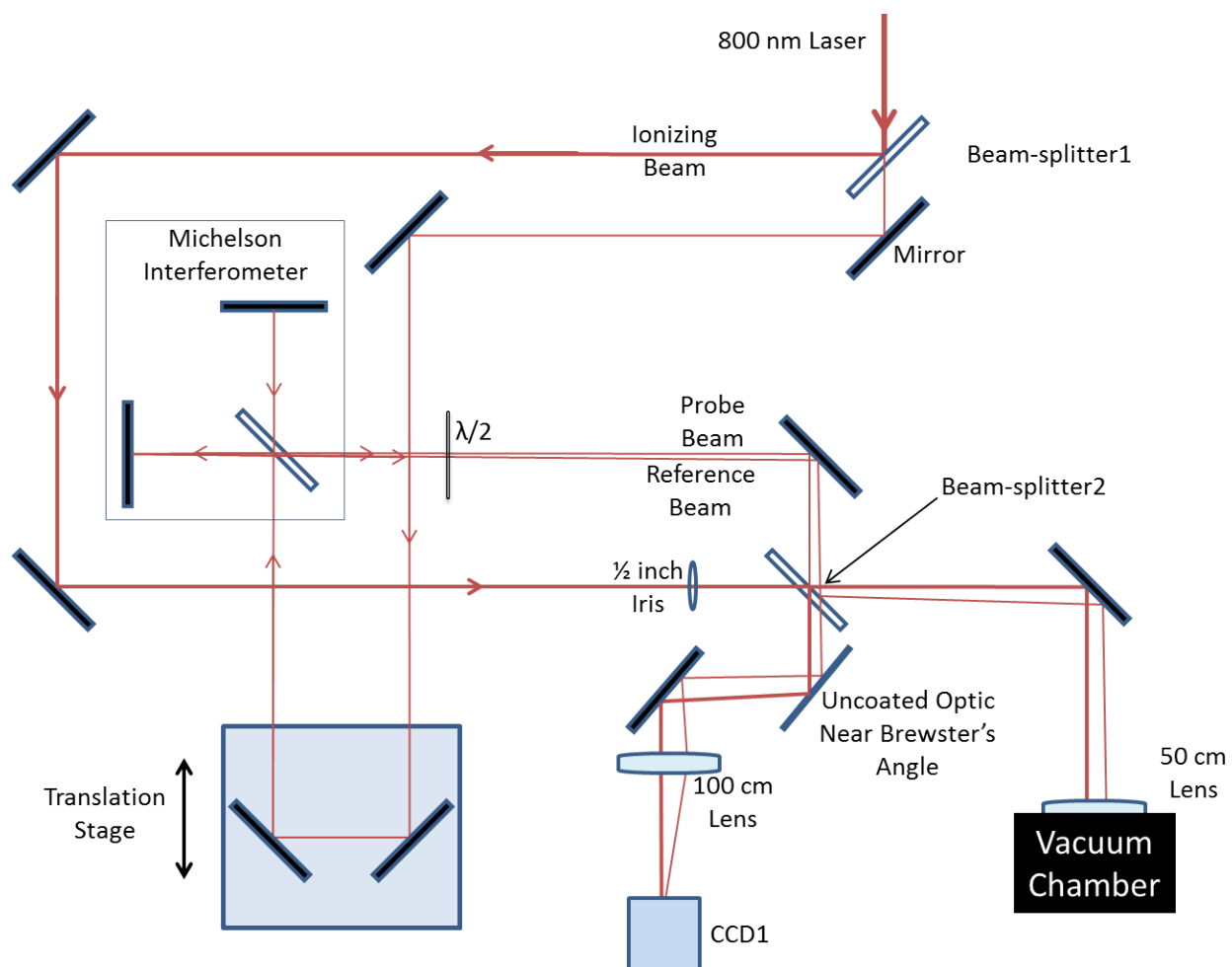


Figure 3.1 The optical setup of the laser system. The original 800 nm pulse is split by a beam splitter, the ionization beam passes through the iris before recombining with the probe/reference beams. The probe and reference beams go through a delay track and slightly misaligned Michelson interferometer. After recombining, all three beams then enter the chamber through the 50 cm lens.

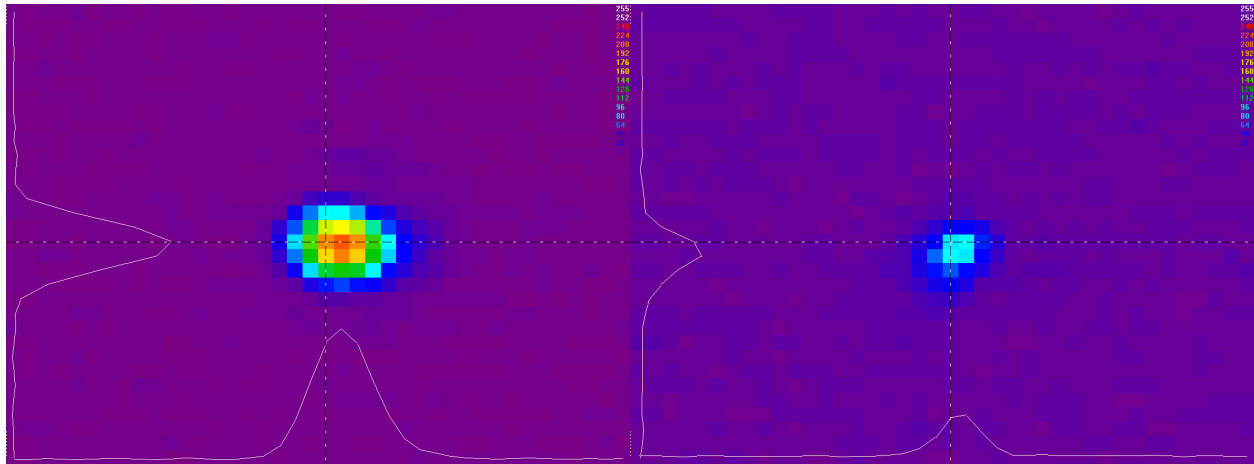


Figure 3.2 The comparable foci of the ionizing and probe beams as seen by the diagnostic CCD. The ionizing beam focus (Left) has vertical and horizontal beam waists of 66.59 and 74.74 μm respectively. The Probe beam focus (Right) has vertical and horizontal beam waists of 44.61 and 53.27 μm

important because the ionizing pulse beam waist at the focus should be larger than the focus of the probe laser beam to avoid systematic errors in the density measurements. The 50:50 beamsplitter (beamsplitter2) is used to recombine the beams before entering the chamber. The rejected beams from the splitter are used for alignment of the foci outside the chamber.

The weaker beam from beamsplitter1 goes through a delay stage on a track system, the Michelson Interferometer, and a half-wave plate. The delay stage allows for relative a delay, adjustable up to approximately 5 ns. The Michelson Interferometer, slightly misaligned, splits the weaker beam equally into probe and reference beams. The probe beam is aligned to focus exactly inside of the ionizing beam's focus, therefore passing fully through the generated plasma. Because of the misalignment, the reference beam focuses above the probe beam about a millimeter outside of the plasma, as depicted in Fig. 3.3. The probe and reference beams both pass through the half-wave plate (waveplate in Fig. 3.1) to switch the polarization before meeting the ionizing beam at beamsplitter2. When these three laser pulses exit the vacuum chamber, they encounter an uncoated optical flat at Brewster's angle, see Fig. 3.3. The horizontally-polarized strong laser beam is com-

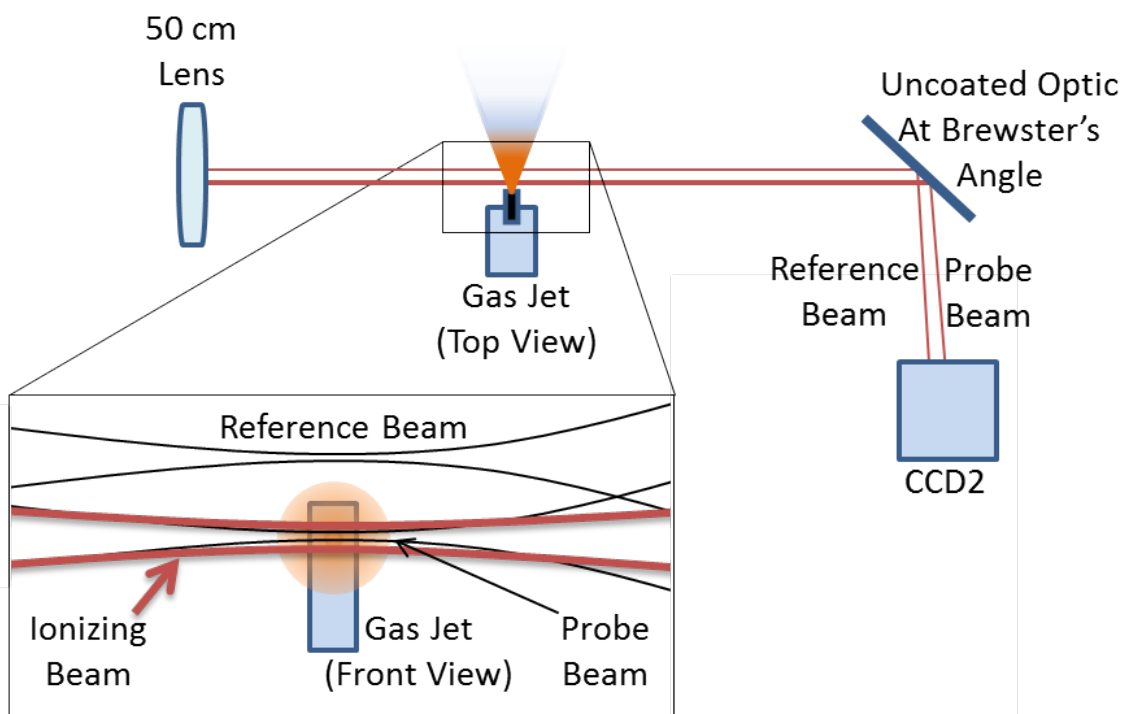


Figure 3.3 The beam pathways within the chamber and afterward. All three beams pass through a 50 cm lens to enter the chamber, where the probe and ionizing beams follow the same path, with the reference beam depicted to the side to show separation from the above view to see placement of gas jet. The front view of the gas jet shows the overlay of all 3 beams, where the center of the gas jet is positioned at the focus of the ionizing beam, shown in red. Where the two black foci are the probe and reference beams. The reference beam is represented here as focusing about, and outside, of the gas jet. After passing the jet all three beams exit the chamber through a window not depicted here as it does not affect the beams. The 3 beams then reflect off an uncoated optic to the CCD2

pletely transmitted through the optical flat. However the weaker vertically polarized probe and reference laser beams are reflected partially from the optical flat and directed towards the measurement CCD (CCD2 in Fig. 3.3). These laser pulses overlap and form fringes that are measured to determine the plasma density.

The three beams that are rejected at beamsplitter2 are used for alignment diagnostics purpose. The three beams are also reflected off an uncoated optic before going through a 100 cm lens to focus at the diagnostic CCD (CCD1 in Fig. 3.1). This allows us to view the focal positions

relative to each other. The uncoated optic is near Brewster's angle to greatly reduce the intensity of the ionizing beam, allowing all three foci to have the same intensity on CCD1 for simultaneous recording. By carefully aligning the ionizing and probe beams, the relative positions of the foci on CCD1 correspond to the relative positions of the foci within the chamber. The foci of the ionizing and probe beams can then be overlapped, the probe entering after being delayed by a chosen amount. This is important because changes in the delay path change the overall beam alignment.

3.2 Vacuum System and Gas Jet

The chamber is cylindrical, approximately 35 cm in diameter and 25 cm deep, with various ports around it, as well as a port on the lid as seen in Fig. 3.4. The beam enters the chamber through a 50 cm lens, shown in Fig. 3.5. The opposite side of the chamber is connected to a long tube to allow the focused beams to expand before exiting through a window for measurements. Perpendicular to the beam path is an xyz -positioner which holds the gas jet, which allows one to position the gas jet relative to the focus of the ionizing beam. Opposite the gas jet is a turbo pump (Balzers, TPU 510) backed by a scroll pump. When the jet is not running the base pressure of the system stabilizes in the 10^{-5} torr range, while when the jet is operating the background pressure in the chamber raises up to about 3×10^{-3} torr, depending on the backing pressure for the jet.

Two of the other ports are also windows which enable jet alignment and troubleshooting by eye. To avoid overloading the turbo pump, there are two pressure sensors fixed next to the pump, allowing us to know the overall pressure in the chamber. The last port has a vacuum tee attached. Through this tee we send the electrical power for the jet. There is also a valve for venting the chamber and tube that feeds gas to the jet. The gas line leads to another tee that is used as another small chamber, as a pressure controlled gas feed for the gas jet.

The gas jet uses an electronically pulsed solenoidal valve (Hargraves, 30 Magnum), which has

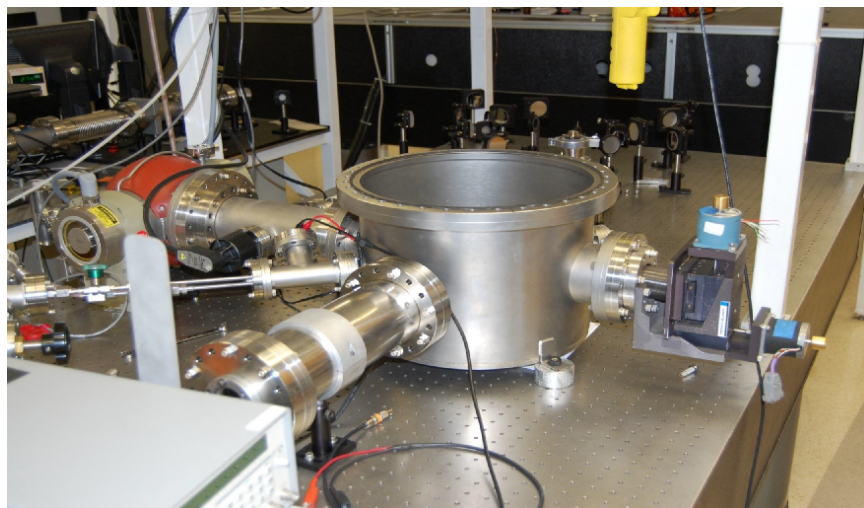


Figure 3.4 Vacuum chamber. The Optical layout in Fig. 2.1 is visible behind the chamber

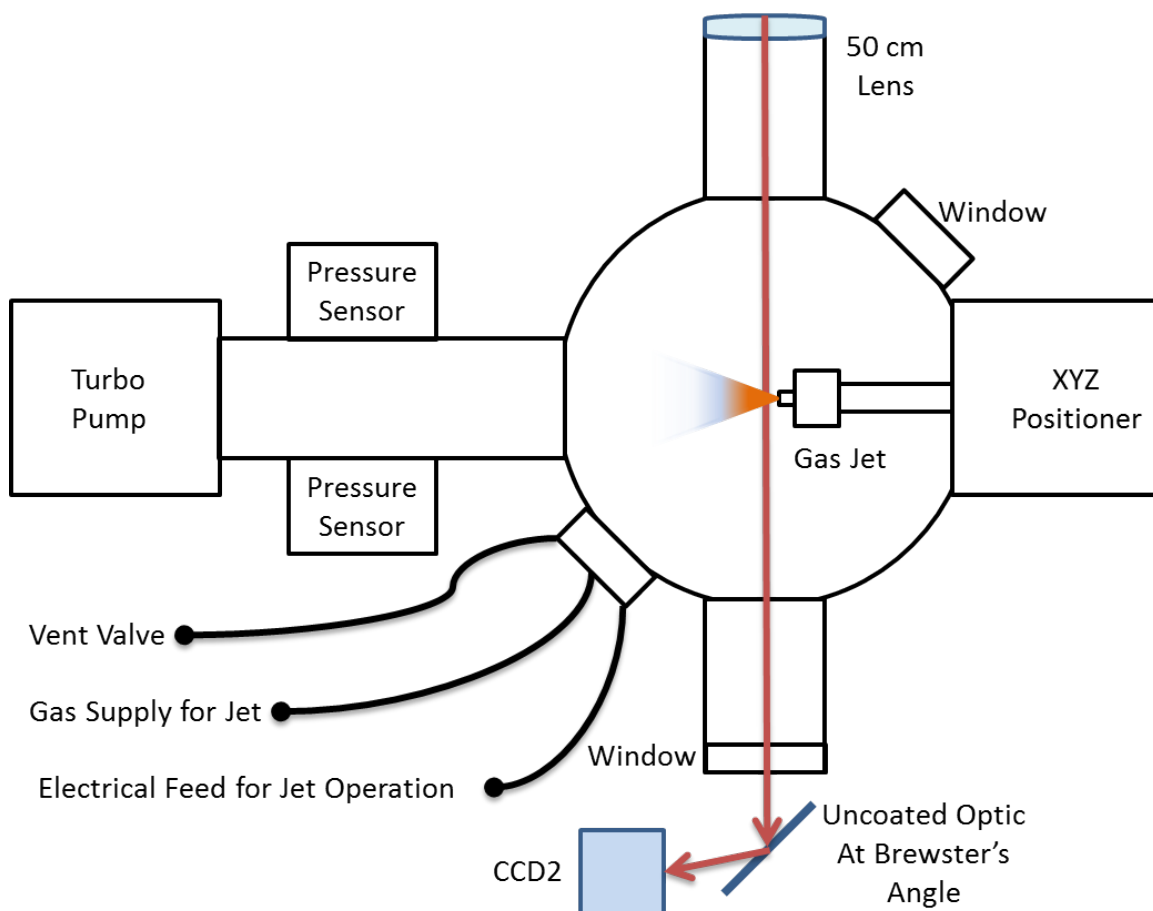


Figure 3.5 The layout of the vacuum chamber.

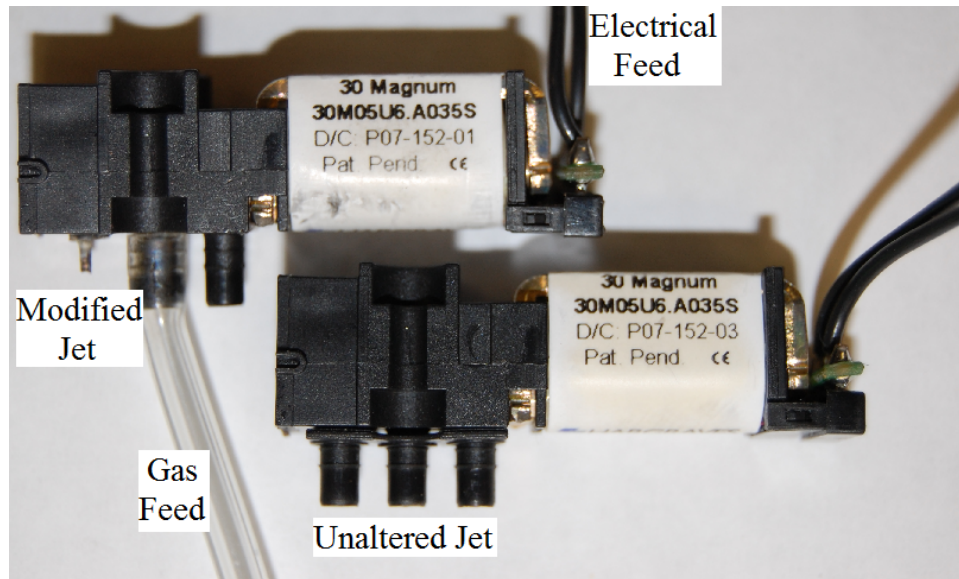


Figure 3.6 Comparison of an unaltered and modified solenoidal valves

been modified so that the feedthrough is no longer a larger plastic port, but a narrow metal needle to produce a narrow jet. The backing pressure for the jet can be varied. In our work we use pressures of 250, 500, and 1000 torr. Although these high pressures are behind the jet, this is not the pressure at the focus of the ionizing beam, which reaches only about 40 torr when backed with 1000 torr. Since the jet is also pulsed and does not run continuously, this allows us to keep the background pressure in the chamber low by matching the duty cycle of the jet to the duty cycle of the laser. Since the solenoidal valve does not respond in the 35 fs range, the pulse width for the jet was minimized to the smallest amount that allowed the valve to open completely before closing again, 5 to 10 ms.

3.3 System Electronics

The 10 Hz repetition rate for the Ti:sapphire amplifier sets the repetition rate for the entire experiment. We send an electronic pulse to open the gas jet a few milliseconds before the laser pulse

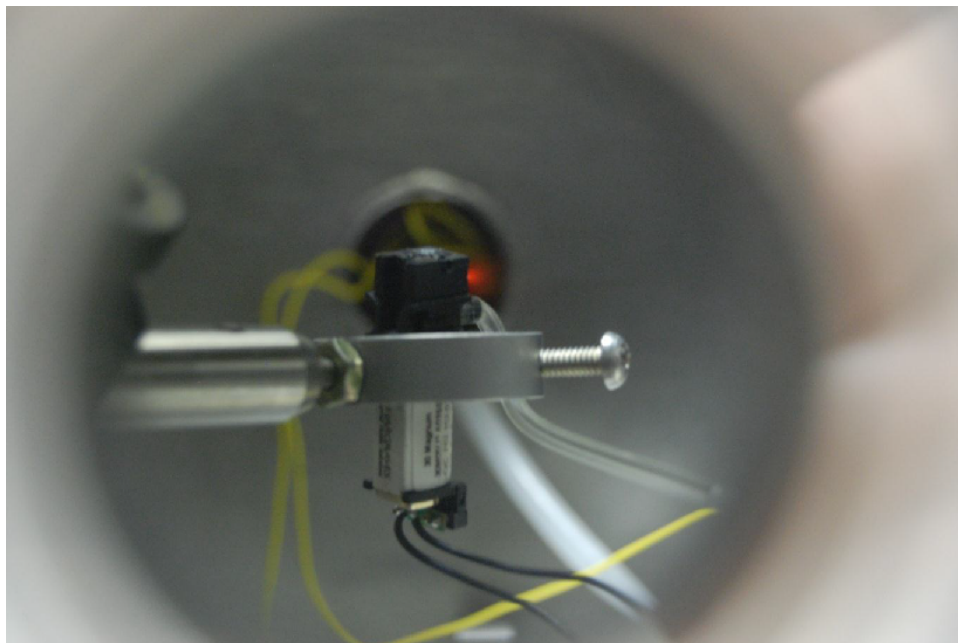


Figure 3.7 Gas jet and plasma from laser ionization, as visible from a window port on the side of the chamber. Opposite the window is the port from Fig. 3.5 that offers the electric and gas feedthroughs for the jet. The gas jet is also represented in Fig. 3.3

arrives. This ensures that the valve in the jet is completely open when the laser pulse arrives. We use two pulse generators to open and close the gas valve based on triggers from the previous laser pulse.

Our pulse generators cannot be triggered while they are sending out a pulse. The first pulse generator (Stanford Research Systems, Model DG535) uses a delay of 94 ms before sending a pulse to the second (Hewlett Packard, Model 214B). After sending the pulse the first pulse generator is available to be triggered while the second generator is delayed the correct amount (about 3 ms) before sending its pulse to open the gas valve so that it is completely open when the laser pulse arrives. The duration of the pulse sent to the jet is approximately 1.6 ms, and the gas jet is open for approximately 5 ms.

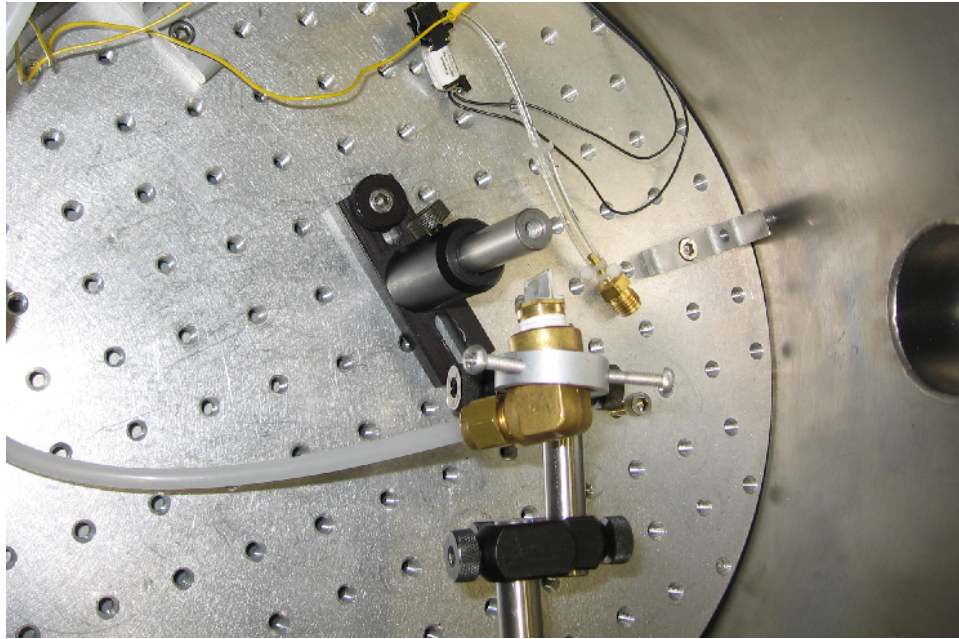


Figure 3.8 Gas Cell as setup within the chamber. The opening on the right is where the focusing beams enter to focus at the position of the cell.

3.4 A Gas Cell for Calibration Purposes

Two challenges arise when using the gas jet: not knowing the actual gas density at the laser focus and not knowing exactly the width of the expanding gas jet. Moreover the position of the tip of the gas jet relative to the focus was not necessarily repeatable on each run. To check the plasma length and density for the calculations on acquired data, a gas cell was used. The cell is a metal frame with a 1 mm thickness molybdenum foil was attached on either side with Torr Seal (see Fig. 3.9). In the cell, both the path length and the pressure are reasonably well known.

Before the experiment begins, the laser drills a hole through both sides of the cell's molybdenum foil. The challenge when using a gas cell is that neither the probe nor reference beams are powerful enough to drill through the foil, meaning the ionizing beam needs to be used to drill two separate holes (prior to the experiment). This is done by positioning the probe and reference beams at the desired positions to overlap the probe and ionizing focus, and then to re-align the



Figure 3.9 Example of Gas Cell with the two drilled holes for the beam paths

ionizing beam to the two desired positions (of the two foci) for a few minutes to drill through both foils. After the holes are drilled and the system is realigned, all three beams pass through the cell. Though the reference beam also passes through gas, only the probe beam goes through gas which has been ionized, so the data acquisition and analysis is unaltered.

With the gas cell the pressure is not pulsed, the flow of gas into the chamber is constant. Having four drilled holes limits the pressure to avoid too much gas flowing into the chamber. This resulted in a maximum operating pressure of 40 torr for our system. If the background pressure in the chamber gets too high then the pressure gauges stop working, making the background pressure unknown. At that point the pressure in the chamber could still be low, but just outside of the gauge range, or getting too high and overtaxing the turbo pump. In spite of these limitations, the known pressure and plasma length in the cell make it possible for us to verify our model and to determine the quantity nL in our experiment.

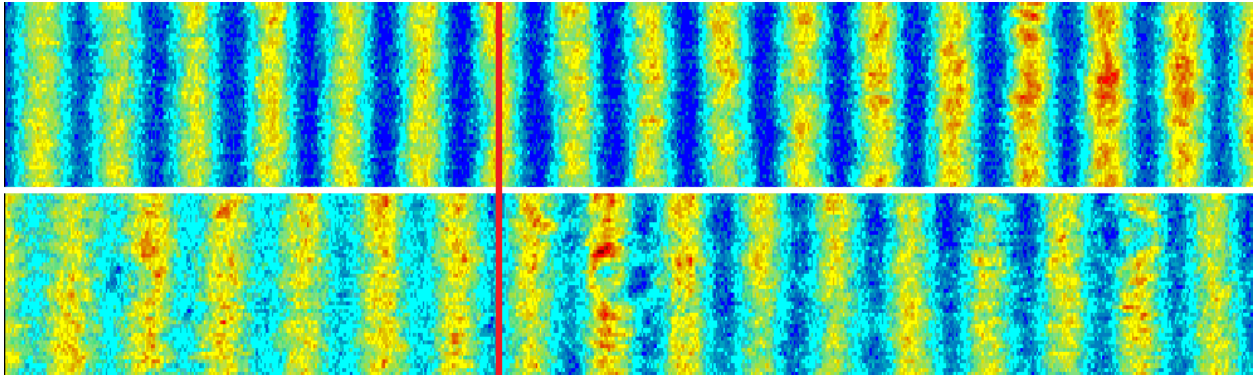


Figure 3.10 Interference fringes in the far field as measured using camera CCD2 shown in Fig. 2.1. The top panel shows the fringes when no plasma is present. The bottom panel shows the fringes when the plasma is present. The data in the bottom panel is taken when the plasma density is $n = 1.3 \times 10^{18} \text{ cm}^{-3}$ at a delay of 100 ps. A fringe shift of about π radians occurs between the top and bottom panels of this figure. Each image is an average of 20 laser pulses.

3.5 Data Acquisition

When the three beams exit the chamber through the window they are reflected off an uncoated optic before hitting CCD2 (Fig. 3.3). The optic is positioned at Brewster's angle to greatly reduce the intensity of the p-polarized ionizing beam, which is no longer needed (because the ionizing beam is oppositely polarized to the probe/reference beams). The probe and reference beam spread out so they overlap, and create interference fringes on CCD2, as can be seen in Fig. 3.10. A simple labview program has been written to view and average images from CCD2.

By blocking or unblocking the ionizing beam before it enters the chamber, the gas jet is either unionized or ionized, respectively. When allowing the ionizing beam into the chamber the fringes are observed to move depending on the index change from the free electrons (see Fig. 3.10). By recording and averaging 20 images of when the ionizing beam is blocked, and another 20 when unblocked, we acquire an accurate shift in the fringe pattern. This was repeated 10 times in quick succession, which offered multiple measurements for error calculations and an estimate of temporal shifts.

Measurements are recorded at various positions of the delay track, changing the delay between the ionizing beam and probe beam. At each delay the number of free electrons changes depending on the recombination rate of the plasma as well as the plasma's expansion. These two factors affect how much the fringes are observed to shift. A measurement is also recorded with a negative delay, so that the probe beam passes through before the ionizing beam, as a check that the fringes are unaffected. At each of these positions, the measurements are taken three times for three different backing pressures of the gas jet, 250, 500, and 1000 torr as mentioned before. This allows us to observe the changes of the plasma over time for three separate starting densities.

To take the measurements as described, a labview program is used. Along with the jet the camera controlled by the program also receives a trigger from the 800 nm laser system for synchronization. The program prompts the user to either block or unblock the ionizing beam in quick succession as it records the data. This is done for each delay position, which the user also enters into the program.

After taking all the measurements and averaging the data, the labview program saves the data. It also names each file according to whether the ionizing beam is blocked, and records the backing pressure and position of the delay line. The file itself is a "space delimited text file" where it records a matrix of numbers for each pixel value in the final image, separated by spaces.

Chapter 4

Data Analysis and Discussion

4.1 The Analysis Matlab Program

A Matlab program (see appendix) is used to analyze the amount of fringe shift and relate that to plasma density. Matlab reads the saved text file, inputting the spaced numbers from each pixel into a matrix array. These array's can then be plotted to reproduce the image recorded in CCD2, as seen in Fig. 4.1.

The first step in the analysis is to average the values of the pixels vertically along the fringe length. The result of this is a sinusoidal plot of the fringe intensity along the x position (see Fig. 4.1). A risk of doing this is a possible compromise to the accuracy of the position if the fringes are slightly slanted when summing vertically, though this does not appear to be a problem in our measurements.

Since the ionizing beam is not completely eliminated by the reflection from the uncoated optic and also the probe/reference beam combination is not uniform over CCD2, the sinusoidal curve is not completely uniform in amplitude. After obtaining the sinusoidal plot of the fringe positions we fit a single parabolic curve to the entire wave, which produces a curve (nearly a straight line)

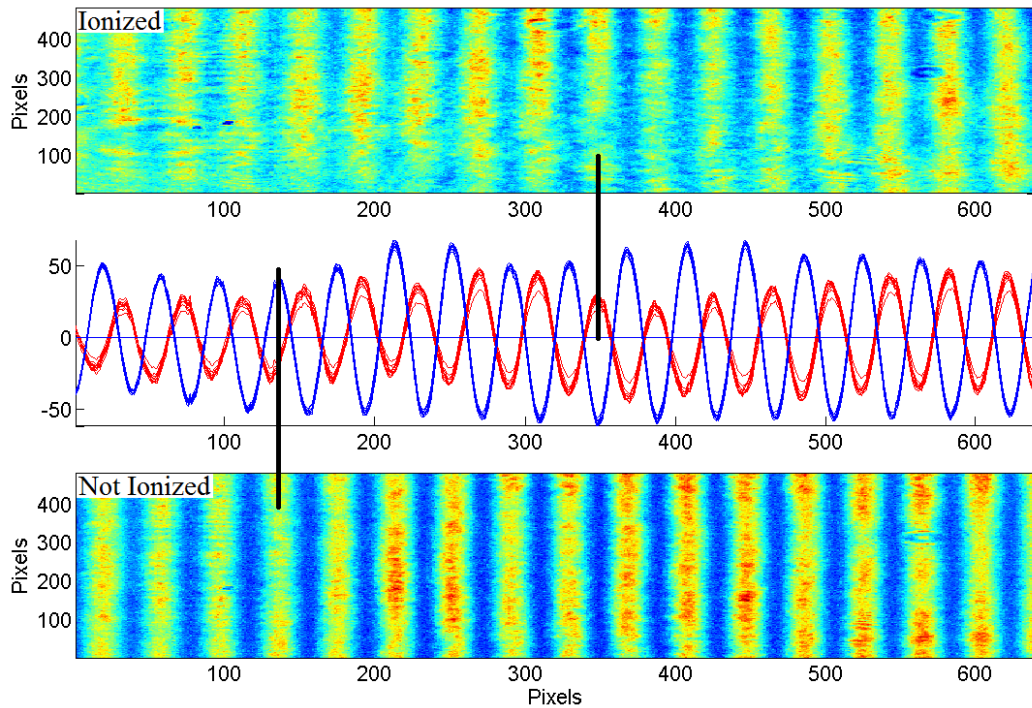


Figure 4.1 The plots from the matlab program

running through the middle of the oscillations. This fit is then subtracted from the wave to remove the background and center the oscillations vertically about zero.

After this background subtraction, we determine the amount the fringes have shifted. Instead of using the locations of the peaks for each fringe, we use the positions of the zeros where the curve crosses the x-axis. By determining how far the zeros-crossings have shifted we can determine the plasma index. By doing this for each fringe we have multiple calculations for the shift which let us estimate error.

Typical data showing the shift in the interferometer fringes is plotted in Fig. 4.2. The fringe shift is measured in pixel number. That number is converted to phase by equating the period of the interference pattern to a phase shift of 2π . The fringe shift is used to determine the index of refraction and the plasma density (see Eq. (2.9)).

We calibrated our measurement using a 1 mm thick gas cell. CCD1 in Fig. 2.1 makes it pos-

sible to place the strong laser focus with high reproducibility. The Ne pressure in the cell is then increased to 50 Torr. Under these conditions we measured a phase shift of approximately π . This verifies the analysis in Eq. (2.9) and that we know the plasma length. Since the plasma density is linearly related to the pressure behind the gas jet, which means that the amount of ionization is independent upon jet pressure. This indicates that we are ionizing essentially all of the atoms within the laser focal volume.

4.2 Results

Our experimental setup makes it possible to measure the plasma density as a function of time and jet backing pressure. Typical results are shown in Fig. 4.2. The multiple plots in each panel relate to the backing pressure for the gas jet, 250, 500, and 1000 torr. The top panel of Fig. 4.2 shows the measured fringe shift in pixels as a function of the distance of the delay arm for three different plasma conditions. The middle panel shows the same data plotted as phase delay vs. time. The bottom panel is the phase delay from the middle panel, divided by the backing pressure for the jet.

It is important to remember that the phase shift $\Delta\phi$ is proportional to the product of the plasma density and the path length, NL (see Eq. (2.9)). In order to extract the plasma density, the length of the plasma must be known. We know the approximate length of 1 mm from the gas cell. Because of the large aspect ratio of the laser focus (50 μm laser waist and ~ 1 mm length), the plasma expands rapidly in the xy -plane. As the plasma adiabatically expands, the electron temperature falls. The bottom panel in Fig. 4.2 shows the data in the upper panel again, but with the plasma density scaled by the peak plasma density. The change, or slope, in the plasma density is independent of the peak density. This indicates that the overall change in the density is due to plasma expansion and not to recombination because recombination processes are density (and temperature) independent.

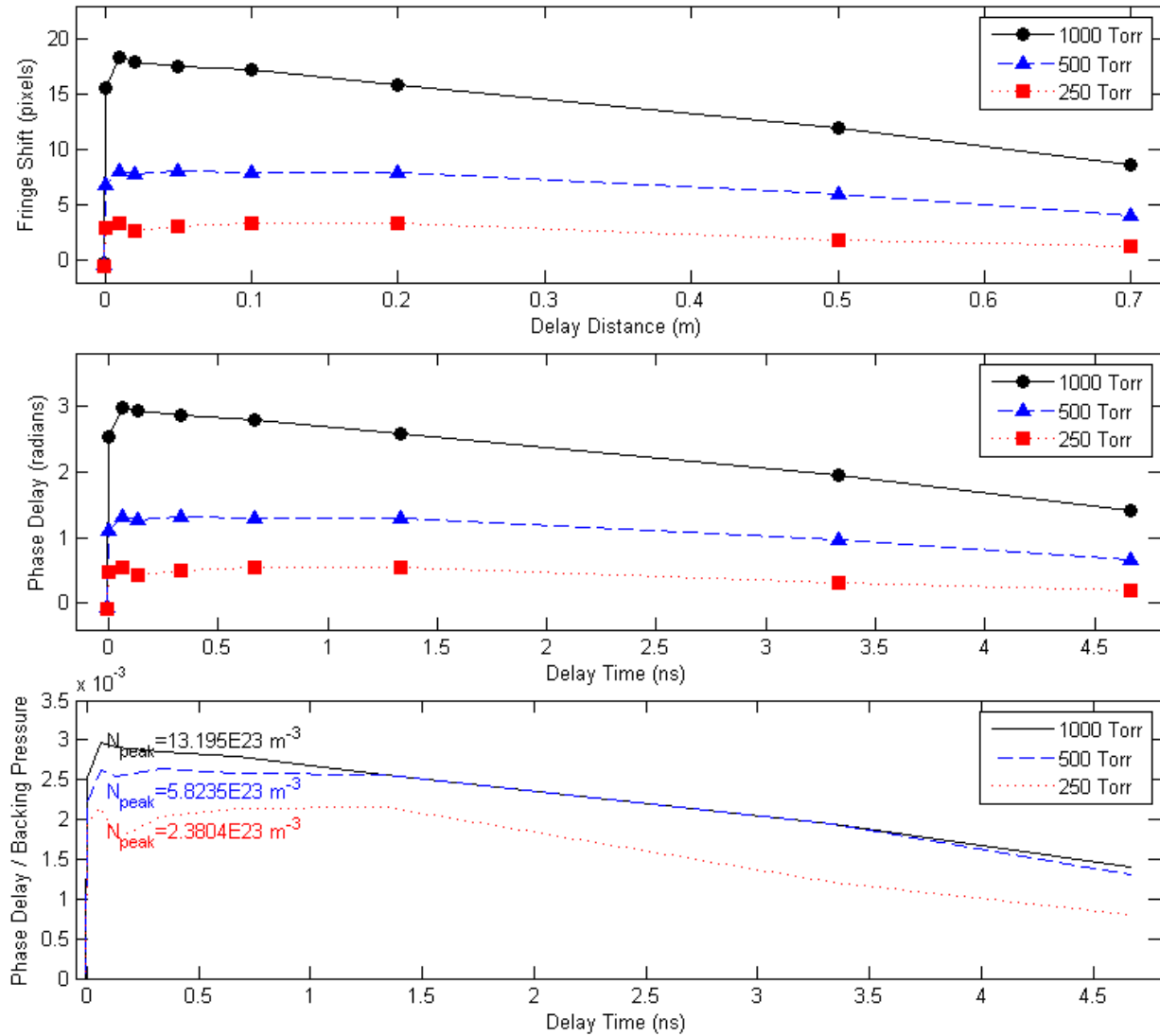


Figure 4.2 The plasma shift and phase delay as a function of time for three different Ne jet backing pressures. The plasma density falls as the plasma expands. The bottom panel shows that this reduction in plasma density is independent of the initial plasma density, suggesting that recombination does not significantly change the plasma density on these time scales. It is expected that as the density increases, the effects of dielectronic and three-body recombination can be measured.

From the density data we can extract the electron temperature of the plasma. This is done by relating the expansion rate curves directly to the model for the UNPs, see Fig. 4.3. As a model from UNPs being used on our laser focus, the rms size σ of the plasma is given by

$$\sigma(t) = \sqrt{\sigma_0^2 + v_{exp}^2 t^2} \quad (4.1)$$

where $v_{exp} = \sqrt{\frac{k_B T_e}{m_i}}$ is the expansion velocity, σ_0 is the initial size, T_e is the electron temperature, and m_i is the mass of the ion. At the laser focus, using the rms size as the beam waist at the center, and a plasma length of L (where ΔL is effectively constant for our measurements as $L \gg \sigma$). With this our equation for plasma density in the laser focus becomes

$$N = \frac{\tilde{N}}{2\pi\sigma^2\sqrt{2\pi L}} e^{-\frac{\rho^2}{2\sigma^2}} e^{-\frac{z^2}{2L^2}} \quad (4.2)$$

where \tilde{N} is the total number of electrons in the plasma, ρ is the radial distance from the center, and z is the distance from center along the length L . By looking at the peak of the density, or density peak, we get

$$N_{pk}(t) = \frac{\tilde{N}}{2\pi L \sqrt{2\pi} \sigma^2(t)} = \frac{N_{pk}(0)}{\sigma^2(t)/\sigma_0^2} = \frac{N_{pk}(0)}{1 + t^2 \frac{v^2}{\sigma_0^2}} = \frac{N_{pk}(0)}{1 + t^2 \frac{k_B T_e}{m_i \sigma_0^2}} \quad (4.3)$$

We can then get our model curve by looking at the ratio of this peak density in time to the initial peak density, giving us the model equation

$$\frac{N_{pk}(t)}{N_{pk}(0)} = \frac{1}{1 + \frac{t^2}{\tau^2}} \quad (4.4)$$

where $\frac{1}{\tau^2} = \frac{k_B T_e}{m_i \sigma_0^2}$ is the fit parameter which is selected to give us a curve that best matches our data. And then from the selected τ that fits the curve best, we can use it to extract an estimated electron temperature

$$T_e = \frac{\sigma_0^2 m_i}{k_B \tau^2} \quad (4.5)$$

In Fig. 4.3 the model fit used gives us an electron temperature of approximately 44 eV.

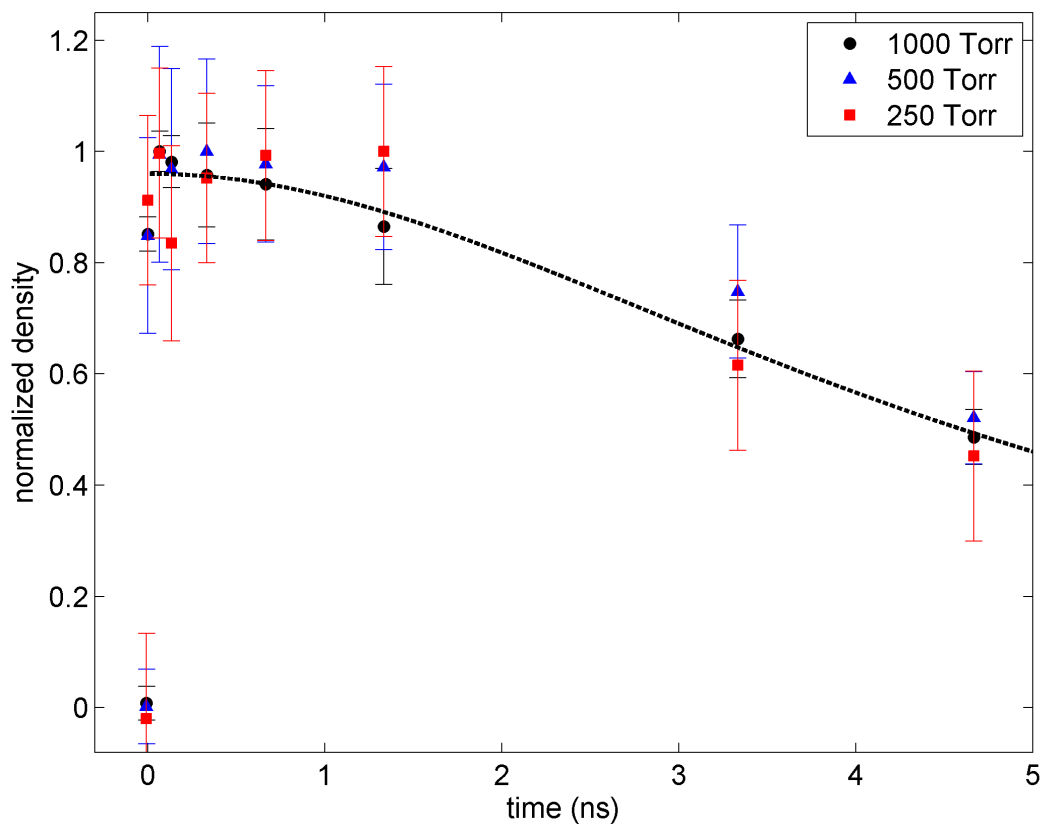


Figure 4.3 A direct relation of the measured data, normalized by the peak values of the each respective data plot. Which are expressed for the 250, 500, and 1000 torr data runs expressed by the points. The black line is the model of the UNPs, Eq. (4.4)

4.3 Conclusion

We have demonstrated a new method for measuring plasma density. The expansion of LPP laser produced plasmas is driven by the electron pressure. We have shown that the analytic solution for the plasma expansion derived for UNPs describes the expansion of our LPPs. Comparing these solutions with data published by Kanter [6] gives us confidence that the expansion data and the UNP model can be used to extract a reliable electron temperature.

We have shown that there is no recombination at early times under our plasma conditions because the electron temperature is so high (see Figs. 4.2 and 4.3). Recombination rate is primarily independent upon the initial starting density, which we have observed for our plasma to be directly related to the backing pressure. But for each pressure the overall curves and expansion rate all follow the same path, indicating that there is no significant recombination in this time frame.

Future studies could try to measure plasma recombination. At high enough densities it should be possible to measure density-dependent recombination rates. If the electron temperature is low enough it may be possible to see the importance of three-body recombination. Studies of UNPs suggest this should happen with an electron strong coupling parameter of $\Gamma \geq 0.1$ where

$$\Gamma = \frac{Z^2 e^2}{4\pi\epsilon_0 a_{ws}} \frac{1}{k_B T_e}. \quad (4.6)$$

Here Z is the ionization state of the plasma ions, $a_{ws} = \left(\frac{3}{4ZD\pi}\right)^{1/3}$ is the Wigner-Seitz radius or average distance between particles in the plasma, D is the ion density, and k_B is Boltzmann's constant. When the electron temperature is low enough, UNPs become non-ideal because the number of particles per Debye sphere can be unity or less. UNPs reach this regime because of low temperatures, in spite of the low plasma density.

For an electron temperature of 5 eV, this should happen at a plasma density of $N = 3 \times 10^{19} \text{ cm}^{-3}$, or a room-temperature density of about 330 Torr. At these high densities, the fringe shift will be very large, 10 times the $\sim \pi$ shift measured in our experiments. This could be un-

raveled by gradually increasing the plasma density and measuring the fringe shift. If the initial plasma density is known, the fringe shift method outlined here gives an accurate way of measuring changes in the density. Future studies could also explore experimental parameters that influence the electron temperature in detail. Systematic studies of its dependence on plasma density, on laser intensity and power, and on ionization state could be carried out. This would provide important insights on how to approach the largely unexplored high- Γ neutral atomic plasmas.

Bibliography

- [1] C. Morgan, “Some aspects of laser-produced plasmas.,” *Plasma Physics and Controlled Fusion* **26**, 1367 (1984).
- [2] S. Banerjee, N. Powers, V. Ramanathan, B. Shadwick, and D. Umstadter, “Stable, monoenergetic 50-400 mev electron beams with a matched laser wakefield accelerator.,” *Proceedings of Particle Accelerator Conference* (2009).
- [3] T. C. Killian, S. Kulin, S. D. Bergeson, L. A. Orozco, C. Orzel, and S. L. Rolston, “Creation of an Ultracold Neutral Plasma.,” *Phys. Rev. Lett.* **83**, 4776–4779 (1999).
- [4] T. Kluge, T. Cowan, A. Debus, U. Schramm, K. Zeil, and M. Bussmann, “Electron temperature scaling in laser interaction with solids.,” *Phys. Rev. Lett.* **107**, 205003 (2011).
- [5] P. Mora, “Plasma expansion into a vacuum.,” *Phys. Rev. Lett.* **90**, 185002 (2003).
- [6] E. P. Kanter *et al.*, “Characterization of the spatiotemporal evolution of laser-generated plasmas,” *APPLIED OPTICS* **104**, 073307 (2008).

Appendix A

Matlab - Data Analysis

```
1 %% Fringe Analysis program – Nathan Heilmann
2 % Brigham Young University – Department of Physics and Astronomy
3
4 clear;
5 close all
6
7 %% Loading all the data into Matlab
8 III1=load('Delay_Pos_2_Ionized+1000_measurement1');
9 BBB1=load('Delay_Pos_2_Blocked+1000_measurement1');
10 III2=load('Delay_Pos_2_Ionized+1000_measurement2');
11 BBB2=load('Delay_Pos_2_Blocked+1000_measurement2');
12 III3=load('Delay_Pos_2_Ionized+1000_measurement3');
13 BBB3=load('Delay_Pos_2_Blocked+1000_measurement3');
14 III4=load('Delay_Pos_2_Ionized+1000_measurement4');
15 BBB4=load('Delay_Pos_2_Blocked+1000_measurement4');
16 III5=load('Delay_Pos_2_Ionized+1000_measurement5');
17 BBB5=load('Delay_Pos_2_Blocked+1000_measurement5');
18 III6=load('Delay_Pos_2_Ionized+1000_measurement6');
19 BBB6=load('Delay_Pos_2_Blocked+1000_measurement6');
20 III7=load('Delay_Pos_2_Ionized+1000_measurement7');
21 BBB7=load('Delay_Pos_2_Blocked+1000_measurement7');
22 III8=load('Delay_Pos_2_Ionized+1000_measurement8');
23 BBB8=load('Delay_Pos_2_Blocked+1000_measurement8');
24 III9=load('Delay_Pos_2_Ionized+1000_measurement9');
25 BBB9=load('Delay_Pos_2_Blocked+1000_measurement9');
26 III10=load('Delay_Pos_2_Ionized+1000_measurement10');
27 BBB10=load('Delay_Pos_2_Blocked+1000_measurement10');
28
29 %% Taking Data and averaging Y values to make fringe location plots
30 II1=mean(III1);    II2=mean(III2);    II3=mean(III3);    II4=mean(III4);
```

```

31 II5=mean(III5);    II6=mean(III6);    II7=mean(III7);    II8=mean(III8);
32 II9=mean(III9);    III10=mean(III10);
33
34 BB1=mean(BBB1);    BB2=mean(BBB2);    BB3=mean(BBB3);    BB4=mean(BBB4);
35 BB5=mean(BBB5);    BB6=mean(BBB6);    BB7=mean(BBB7);    BB8=mean(BBB8);
36 BB9=mean(BBB9);    BB10=mean(BBB10);
37
38 % Fitting a polynomial to the central path of the averaged data
39 x=1:640; y=0*x;
40 ftI1=polyfit(x,II1,2);    ftI2=polyfit(x,II2,2);    ftI3=polyfit(x,II3,2);
41 ftI4=polyfit(x,II4,2);    ftI5=polyfit(x,II5,2);    ftI6=polyfit(x,II6,2);
42 ftI7=polyfit(x,II7,2);    ftI8=polyfit(x,II8,2);    ftI9=polyfit(x,II9,2);
43 ftI10=polyfit(x,II10,2);
44
45 ftB1=polyfit(x,BB1,2);    ftB2=polyfit(x,BB2,2);    ftB3=polyfit(x,BB3,2);
46 ftB4=polyfit(x,BB4,2);    ftB5=polyfit(x,BB5,2);    ftB6=polyfit(x,BB6,2);
47 ftB7=polyfit(x,BB7,2);    ftB8=polyfit(x,BB8,2);    ftB9=polyfit(x,BB9,2);
48 ftB10=polyfit(x,BB10,2);
49
50 % Centering Y values on the zero
51 I1=II1-polyval(ftI1,x);    I2=II2-polyval(ftI2,x);    I3=II3-polyval(ftI3,x);
52 I4=II4-polyval(ftI4,x);    I5=II5-polyval(ftI5,x);    I6=II6-polyval(ftI6,x);
53 I7=II7-polyval(ftI7,x);    I8=II8-polyval(ftI8,x);    I9=II9-polyval(ftI9,x);
54 I10=II10-polyval(ftI10,x);
55
56 B1=BB1-polyval(ftB1,x);    B2=BB2-polyval(ftB2,x);    B3=BB3-polyval(ftB3,x);
57 B4=BB4-polyval(ftB4,x);    B5=BB5-polyval(ftB5,x);    B6=BB6-polyval(ftB6,x);
58 B7=BB7-polyval(ftB7,x);    B8=BB8-polyval(ftB8,x);    B9=BB9-polyval(ftB9,x);
59 B10=BB10-polyval(ftB10,x);
60
61 %% Finding locations where plots cross the zero
62 j1=1; j2=1; j3=1; j4=1; j5=1; j6=1; j7=1; j8=1; j9=1; j10=1;
63 for n=1:639 %Range of Top one - Ionized
64     T1=I1(n)*I1(n+1);    if T1<0;    zerosI(j1,1)=n;    j1=j1+1;    end
65     T2=I2(n)*I2(n+1);    if T2<0;    zerosI(j2,2)=n;    j2=j2+1;    end
66     T3=I3(n)*I3(n+1);    if T3<0;    zerosI(j3,3)=n;    j3=j3+1;    end
67     T4=I4(n)*I4(n+1);    if T4<0;    zerosI(j4,4)=n;    j4=j4+1;    end
68     T5=I5(n)*I5(n+1);    if T5<0;    zerosI(j5,5)=n;    j5=j5+1;    end
69     T6=I6(n)*I6(n+1);    if T6<0;    zerosI(j6,6)=n;    j6=j6+1;    end
70     T7=I7(n)*I7(n+1);    if T7<0;    zerosI(j7,7)=n;    j7=j7+1;    end
71     T8=I8(n)*I8(n+1);    if T8<0;    zerosI(j8,8)=n;    j8=j8+1;    end
72     T9=I9(n)*I9(n+1);    if T9<0;    zerosI(j9,9)=n;    j9=j9+1;    end
73     T10=I10(n)*I10(n+1); if T10<0;    zerosI(j10,10)=n;    j10=j10+1;    end
74 end
75
76 k1=1; k2=1; k3=1; k4=1; k5=1; k6=1; k7=1; k8=1; k9=1; k10=1;
77 for n=1:639 %Range of Bottom One - Blocked
78     T1=B1(n)*B1(n+1);    if T1<0;    zerosB(k1,1)=n;    k1=k1+1;    end
79     T2=B2(n)*B2(n+1);    if T2<0;    zerosB(k2,2)=n;    k2=k2+1;    end
80     T3=B3(n)*B3(n+1);    if T3<0;    zerosB(k3,3)=n;    k3=k3+1;    end

```

```

81     T4=B4(n)*B4(n+1);    if T4<0;    zerosB(k4,4)=n;    k4=k4+1;    end
82     T5=B5(n)*B5(n+1);    if T5<0;    zerosB(k5,5)=n;    k5=k5+1;    end
83     T6=B6(n)*B6(n+1);    if T6<0;    zerosB(k6,6)=n;    k6=k6+1;    end
84     T7=B7(n)*B7(n+1);    if T7<0;    zerosB(k7,7)=n;    k7=k7+1;    end
85     T8=B8(n)*B8(n+1);    if T8<0;    zerosB(k8,8)=n;    k8=k8+1;    end
86     T9=B9(n)*B9(n+1);    if T9<0;    zerosB(k9,9)=n;    k9=k9+1;    end
87     T10=B10(n)*B10(n+1); if T10<0;    zerosB(k10,10)=n;    k10=k10+1;    end
88 end
89
90 %% Plotting
91
92 % First Plot is one of the Ionized images for Reference
93 subplot(3,1,1); pcolor(III1); shading flat; ylabel('Ionized');
94
95 % This is the 3rd plot, Bolcked beam image, also reference
96 subplot(3,1,3); pcolor(BBB1); shading flat; ylabel('Blocked');
97
98 % This is middle plot, overlaid plots for reference and managing
99 subplot(3,1,2);
100 hold on;
101 % The red lines are with Ionized Gas
102 plot(I1, 'r'); plot(I2, 'r'); plot(I3, 'r'); plot(I4, 'r'); plot(I5, 'r');
103 plot(I6, 'r'); plot(I7, 'r'); plot(I8, 'r'); plot(I9, 'r'); plot(I10, 'r');
104
105 % The Blue lines are without the Ionized Gas
106 plot(B1, 'b'); plot(B2, 'b'); plot(B3, 'b'); plot(B4, 'b'); plot(B5, 'b');
107 plot(B6, 'b'); plot(B7, 'b'); plot(B8, 'b'); plot(B9, 'b'); plot(B10, 'b');
108 axis tight
109 plot(x,y);
110 hold off
111
112 %% Finding the size of the fringe and fringe shift from zeros
113
114 % Determining the size from one fringe to another in pixels
115 r=size(zerosI,1)-2;
116 for n=1:10;
117     t=1;
118     for m=1:r;
119         fringeI(t,n)=zerosI(m+2,n)-zerosI(m,n);
120         fringeB(t,n)=zerosB(m+2,n)-zerosB(m,n);
121         t=t+1;
122     end
123 end
124
125 % Number of pizels from one fringe to another in matrix form
126 sizeIM=fringeI;
127 sizeBM=fringeB;
128 sizedifM=fringeI-fringeB;
129
130 % Shift in pixels in matrix form

```



```
131 shiftM=zerosI-zerosB;
132
133 % Changing the matrices into row vectors for analysis
134 r=size(zerosI,1);
135 t=1;tt=1;
136 for n=1:10;
137     for m=1:r-2;
138         sizeIR(t)=sizeIM(m,n);
139         sizeBR(t)=sizeBM(m,n);
140         t=t+1;
141     end
142     for m=1:r;
143         shiftR(tt)=shiftM(m,n);
144         tt=tt+1;
145     end
146 end
147 N=size(shiftR,2);
148 NN=size(sizeIR,2);
149 NNN=size(sizeBR,2);
150 display ('Average pixels - Standard deviation - Uncertainty (dev/sqrt(N))')
151 shift(1)=mean(shiftR); shift(2)=std(shiftR); shift(3)=shift(2)/sqrt(N)
152 sizeI(1)=mean(sizeIR); sizeI(2)=std(sizeIR); sizeI(3)=sizeI(2)/sqrt(NN)
153 sizeB(1)=mean(sizeBR); sizeB(2)=std(sizeBR); sizeB(3)=sizeB(2)/sqrt(NNN)
```